Microstructure evolution in undercooled $Co_{80}Pd_{20}$ alloys

**Shengyin Zhou · Rui Hu · Li Jiang ·
Jinshan Li · Hongchao Kou · Hui Chang ·
Lian Zhou**

Abstract High undercooling has been achieved in $Co_{80}Pd_{20}$ melts by employing the method of molten glass denucleating combined with cyclic superheating, and the microstructure evolution with undercooling was systematically investigated. Within the achieved range of undercooling, 0–415 K, two kinds of grain refinements have been observed in the solidification microstructures. The three critical undercoolings are 72, 95, and 142 K, respectively. When undercooling is less than 72 K, the coarse dendritic morphology is formed, which is similar to the conventional as-cast microstructure. The first grain refinement occured in the range of undercooling, 72–95 K can be attributed to the breakup of dendrite-skeleton owing to remelting. When undercooling locates within 95–142 K, highly developed directional fine dendrite can be obtained because the severe solute trapping weakens the effect of solute diffusion during the dendrite growth. The second grain refinement occurred when undercooling exceeds the critical undercooling ($\Delta T^* = 142$ K), the formation of fined equiaxed microstructure can be ascribed to the stress that originates from the extremely rapid solidification process, which resulted in the dendrite fragmentation finally.

Introduction

Much interest has been focused on microstructural evolution in undercooled pure metals and alloys for several decades [1]. Since the first detection of grain refined process in undercooled Ni melts by Walker [2] in 1956, the similar microstructure evolution has been observed in a wide range of metallic systems [3–6]. Various mechanisms have been proposed to interpret the phenomenon, such as copious homogeneous nucleation induced by the collapse of shrinkage cavities [7], dendrites remelting [8], stress-induced broken up and recrystallization [9], fluid flow effects [10], relationship between breakup time and post-recalescence time [3, 11], and the development of growth instabilities [12].

To date, the microstructure evolution in undercooled single phase alloys has been widely investigated, two kinds of grain refinements have been found in many metallic systems [3, 9, 13–15]. It is commonly argued that the grain refinement at low undercooling results from the primary dendrite remelting, but there is no accordant argumentation about the origin of the remelting. Karma [11] proposed a model demonstrated that the break-up of dendrites under the action of remelting causes the grain refinement both at low and high undercoolings, and the occurrence of remelting depends on comparing two times: the time for break up of the dendrites to occur, Δt_{bu}, and the plateau duration, Δt_{pl}, which is the time it takes for the interdendritic melt to completely solidify after recalescence. However, this model uniquely attributed the remelting to the liquid/solid interface tension, ignoring the action of the chemical superheating in the temperature recalescence, whereas the latter may play a more important role in the dendrite remelting, and has a stronger influence on the eventual crystal morphology. Considering
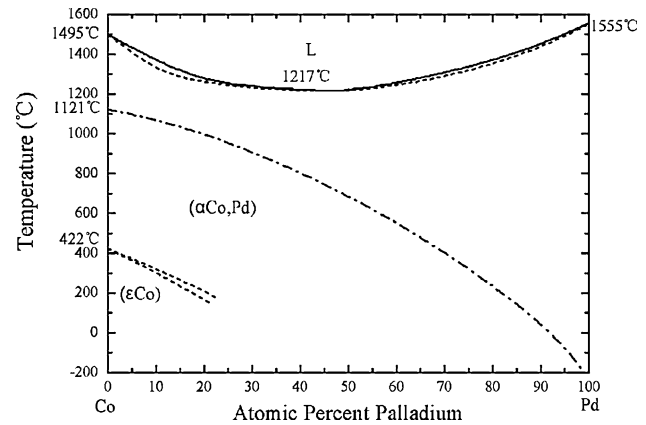
S. Zhou · R. Hu (✉) · L. Jiang · J. Li · H. Kou · H. Chang · L. Zhou
State Key Laboratory of Solidification Processing, Northwestern Polytechnical University, Xi'an 710072, China
e-mail: rhu@nwpu.edu.cn

the action of the chemical superheating in the temperature recalescence, Li et al. [14] pointed out that the dimensionless superheating of the central part of the dendrites stems (i.e., the initially frozen solid) in recalescence could be used to evaluate the dendrite remelting. After a quantitative calculation of the superheating of the primary solid during recalescence, the results indicated that for a single phase alloy with a certain equilibrium solidification temperature interval, the severest remelting should occur in a low-undercooling range, but at high undercooling the superheating has been too low to remelt the dendrite. At present, a large number of researches indicate that there is as yet no uniform argument about the grain refinement at high undercooling. With the development of research, the high stress produced during the rapid solidification at high undercooling attracts popular interests. It probably plays an important role in the dendrite fragment, which has a strong influence on the eventual microstructure [14, 16]. However, details of the influence of stress on the eventual microstructure, such as whether the stress induced recrystallization or merely broke up the initial dendrites, are still unclear.

Usually, for metals or alloys, the melting temperature (T_m) is much higher than the Curie temperature (T_C); the long-range magnetic order is restricted in solid state [17]. Figure 1 shows the phase diagram of Co–Pd binary alloy [18], and the system exhibits the smallest ratio of ΔT_{LC} and T_L, for instance, for $Co_{80}Pd_{20}$, the ratio of ΔT_{LC} and T_L is about 0.21 [17], which lies within the experimentally accessible range of undercooling. At the same time, the completely miscible binary alloy, characterized by phase diagrams with concavous liquidus and solidus lines, exhibits the heat-of-fusion values considerably lower than calculated assuming ideal solution behavior. As a consequence, these metallic systems offer the possibility to achieve the hypercooling regime at a reduced extent of undercooling [19]. However, whether the $Co_{80}Pd_{20}$ melts can be undercooled below T_C or not, i.e., whether the onset of magnetic long range order will stimulate crystal nucleation or not is controversial [17, 20–22]. Based on the above description, $Co_{80}Pd_{20}$ alloy is the optimum system for undercooling below the Curie temperature. The present research about the solidification of undercooled $Co_{80}Pd_{20}$ alloy mainly focused on the following aspects: nucleation behavior [17, 20], undercoolability [19, 23], and physical properties [24, 25] of the undercooled melt. However, there are few reports about the solidification microstructure of undercooled $Co_{80}Pd_{20}$ alloy.

In the present article, high undercooling was achieved in $Co_{80}Pd_{20}$ completely miscible alloy melt by employing the method of molten glass denucleating combined with cyclic

Fig. 1 Phase diagram of Co–Pd binary alloy

superheating, and the microstructure evolution of undercooled $Co_{80}Pd_{20}$ alloys was systematically investigated.

Experimental procedures

The $Co_{80}Pd_{20}$ master alloy ingots were prepared from Co (99.9% purity) and Pd (99.95% purity) by arc-melting under a Ti-gettered argon atmosphere. The ingots were turned over and remelted four times in order to achieve completely homogenized ingots. The as-cast ingot was cut into segments weighing about 5 g for undercooling experiment.

The undercooling experiment was conducted by glass fluxing method in a high frequency induction unit with a coil mounted in atmosphere. The glass flux was B_2O_3 which had dehydrated at 1273 K for 10 h in advance. In each experiment, the alloy together with 2 g glass was contained in a quartz crucible of 10 mm diameter. Then the crucible was placed in a foam alumina base surrounded by the induction coil. As temperature increases, the glass was molten by the heat released from the metal, enwrapping the metal and protecting it from oxidation. Once a desired undercooling was achieved by cyclic superheating, primary solidification was initiated by manual triggering, and then the remaining melts cooled down naturally. The thermal behavior of samples was monitored by an infrared pyrometer with 5 K accuracy and 10 ms response time.

The solidified samples were sectioned longitudinally, processed according to the standard metallographic procedure, and etched with mixed solution (2 mL hydrogen peroxide and 40 mL hydrochloric acid solution). The solidification microstructures of different undercoolings were analyzed by means of optical microscope (OM) and scan electron microscope (SEM). The transmission electron microscope (TEM) was employed to analyze the

sub-microstructure in the grains. Sample preparation for TEM was done by mechanical grinding and ion beam thinning.
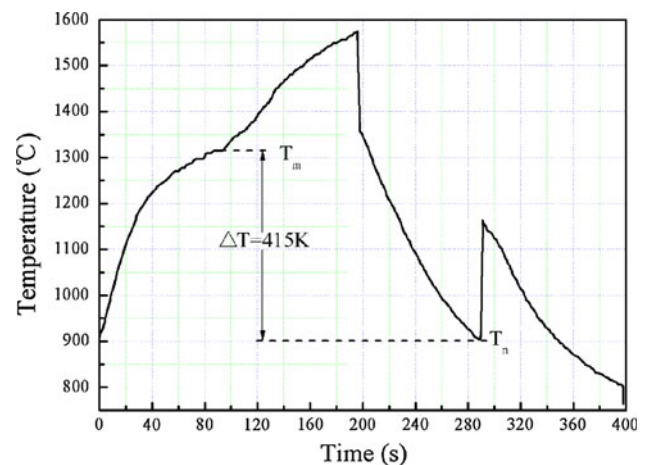
Results

In present case, the highest undercooling achieved in $Co_{80}Pd_{20}$ alloy is 415 K. It indicates that the $Co_{80}Pd_{20}$ melt has been undercooled below T_C into the regime where magnetic ordering will set in. There is a controversial discussion whether the onset of magnetic long range order in $Co_{80}Pd_{20}$ alloy will stimulate crystal nucleation or not. Schenk et al. [20, 22] proposed that the onset of magnetic ordering stimulates crystal nucleation at the undercooling temperature close to T_C is reached, but the reference [21] reported that the Co–Pd melts have achieved sufficient undercooling below T_C. Furthermore, in reference [17], based on the calculation of the magnetic contribution influence on the Gibbs free energy of nucleation, it expressly point out that "In the light of these findings, pure Co and Co–Pd alloys with a very high Co content appear especially suitable for achieving undercoolings below T_C." To sum up the above arguments, magnetic order will influence the nucleation process ascribe to the magnetic contribution on the Gibbs free energy of nucleation, but not explicitly excluded the possibility that the $Co_{80}Pd_{20}$ can be undercooled below T_C. In addition, especially when approaching the T_C, the effects of electromagnetic disturb on the melt cannot be neglected. The onset of magnetic ordering triggers nucleation more likely to occur in the electromagnetic levitation process due to the interaction between the inner magnetic ordering and the external magnetic field. However, in our experiments, the melts in a non-magnetic environment during the cooling stage, the effect of electro-magnetic disturb on the melt is negligible. So an extension of the undercooling below T_C has achieved. Based on the above analysis, we conclude that the onset of magnetic long range order in $Co_{80}Pd_{20}$ alloy will influence crystal nucleation, but the Co-Pd melts can be undercooled below T_C, and it was forcibly confirmed by our experiment.

Figure 2 presents a typical temperature–time profile measured during an undercooling experiment. The melting temperature (T_m), nucleation temperature (T_n), and the undercooling (ΔT) can be seen clearly in Fig. 2. The solidification of undercooled $Co_{80}Pd_{20}$ melt can be described as follows. Once the melt is undercooled to the nucleation point, dendrites form and propagate rapidly through the volume of the melt, and then the rapid release of heat of fusion during dendrite growth leads to temperature rise and rapid recalescence, thus resulting in remelting of the dendrite network. Thereafter, the remaining
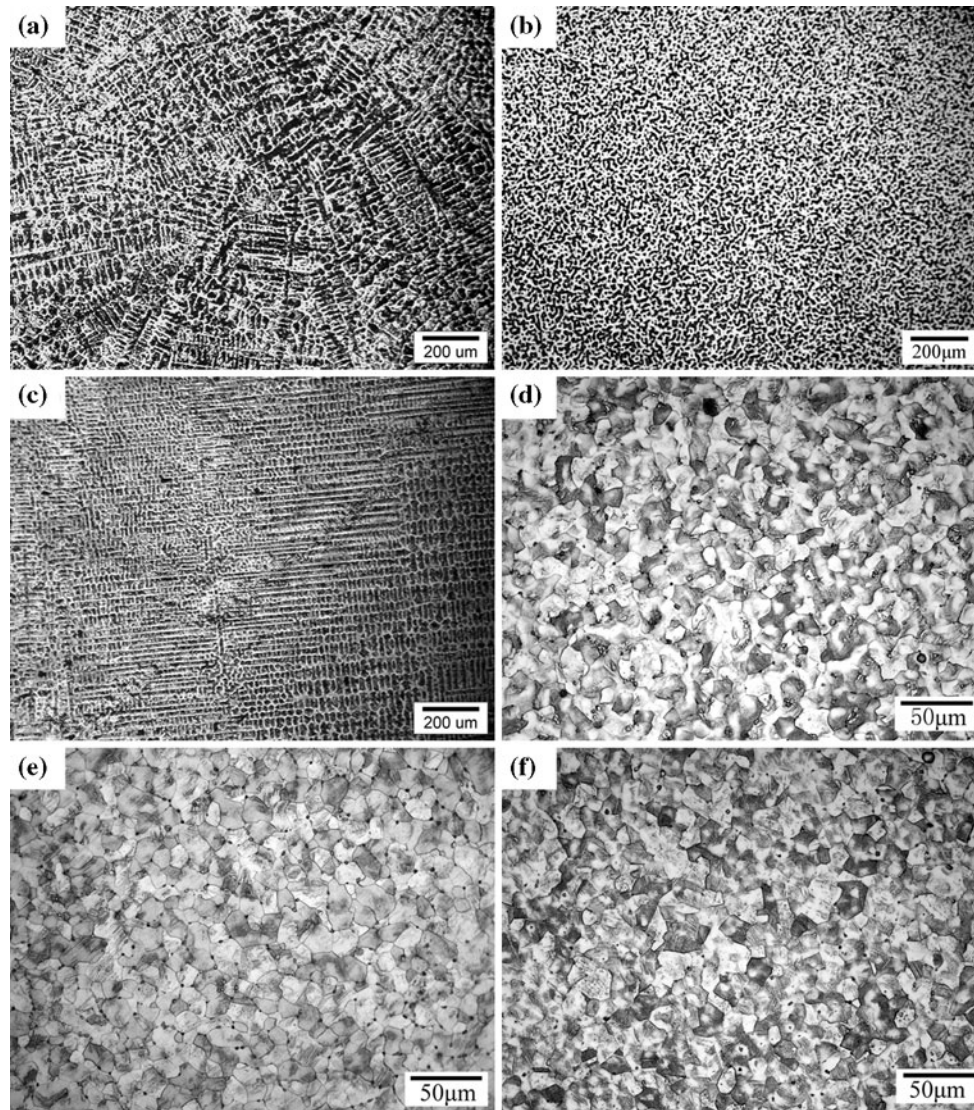
interdendritic liquid starts to solidify onto the dendritic network at low undercooling in post-recalescence. The as-solidified morphologies subject to various undercoolings are shown in Fig. 3. With undercooling increasing, the alloy undergoes two grain refinements: one occurs at low undercooling, and the other at high undercooling, as compatible with the phenomenon observed in other single phase alloys, such as Ni–Cu [14, 26], $Fe_{70}Co_{30}$ [27] and DD3 superalloy [9]. The grain size as a function of initial undercooling (ΔT) is shown in Fig. 4. The characteristic undercooling ΔT_{C1}, ΔT_{C2}, and ΔT_{C3} are 72, 95, and 142 K, respectively.

Corresponding to the three characteristic undercoolings, the microstructure can be classified into four typical morphologies. Once the melt is suffered to a small degree of undercooling ($\Delta T < \Delta T_{C1}$), coarse dendrites with cross-branching are formed (Fig. 3a), which is similar to the conventional as-cast structures. For the sample nucleated at a certain undercooling in the range of ΔT_{C1}–ΔT_{C2}, the overall cross-section is occupied by ripening fragmented dendrite arms, the aforementioned coarse dendrites transform into refined granular grains (Fig. 3b). However, a further increase of undercooling leads to the rise of grain size again. During ΔT_{C2}–ΔT_{C3}, the microstructure consists of the developed directional fine dendrites (Fig. 3c), and the dendrite primary arm spacing decreases with the increase of undercooling (Fig. 4). When $\Delta T > \Delta T_{C3}$, the overall microstructure is refined again, the aforementioned dendritic microstructure is fully substituted by equiaxed crystals with average grain size less than 30 μm (Figs. 3d, e, f, 4), in which many sub-microstructures are found (Fig. 3d, e, f). Further analysis validates that the sub-microstructures are stacking faults. With undercooling increasing, the grain boundaries become sharper, straighter, and more distinct.
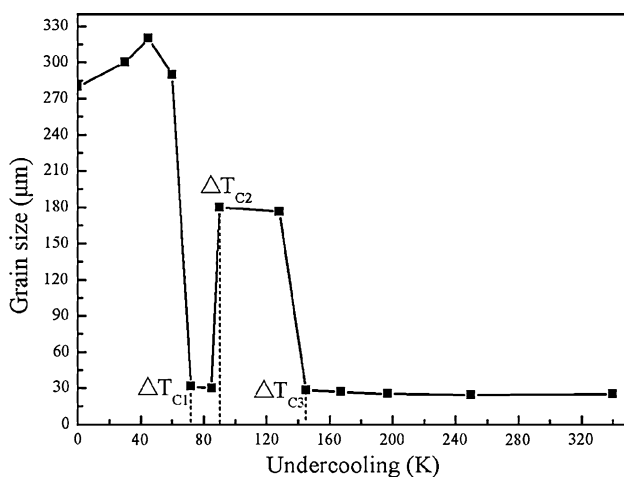

Fig. 2 Temperature-time profile measured on an undercooled $Co_{80}Pd_{20}$ alloy (T_m, melting temperature; T_n, nucleation temperature; ΔT, undercooling)

Fig. 3 Typical microstructure of $Co_{80}Pd_{20}$ alloy with undercooling of 30 K (**a**), 72 K (**b**), 95 K (**c**), 165 K (**d**), 254 K (**e**), 360 K (**f**)

Fig. 4 Grain sizes as a function of undercoolings

Discussion

Dendrites break up model

During the post-recalescence period, the dendrites formed in the recalescence will be subject to serious superheating and will tend to break up. Based on the assumptions that fragmentation of dendrite trunks is driven by both the capillary force and the supersaturation of solute inside the trunk, Karma [11] proposed a model to evaluate the dendrite breakup time (Δt_{bu}), and suggested that if Δt_{bu} is shorter than the plateau duration time (Δt_{pl}), grain refinement will occur.

According to the Karma's model, Δt_{bu} can be calculated by equation (1),

$$\Delta t_{bu} \approx \frac{3}{2} \frac{R(\Delta T)^3}{d_0 D_C} \left| \frac{m_l c_0 (1 - k_e)}{\Delta H_f / C_p} \right| \qquad (1)$$

where m_l, c_0, k_e, ΔH_f, C_p, and D_C are the equilibrium liquidus slope, the alloy composition, the equilibrium partition coefficient, the heat of fusion, the specific heat, and the solute diffusivity in the liquid, respectively. d_0 ($= \Gamma C_p / \Delta H_f$) is the capillary length and Γ is the Gibbs–Thomson coefficient.

Since the trunk radius $R(\Delta T)$, as a function of ΔT, is proportional to the dendrite tip radius $R_{tip}(\Delta T)$, the value of $R(\Delta T)/R_{tip}(\Delta T)$ is approximately 20 [3], applying dendrite growth theory, e.g., BCT model [27], the value of $R_{tip}(\Delta T)$ can be given, and in turn, for $R(\Delta T)$. On this basis, Δt_{bu} can be calculated using Eq. 1 with the thermodynamic parameters given in Table 1. The calculated Δt_{bu} and Δt_{pl} obtained from experiment as a function of undercooling are shown in Fig. 5. The break up time intersects the experimental plateau duration at three ΔT that equal 32, 75, and 142 K. $\Delta t_{bu} < \Delta t_{pl}$ in the undercooling ranges 32–75 K and $\Delta T > 142$ K, according to the view of Karma on the grain refinement mechanism, indicating that there is enough time for the dendrites to break up and grain refinement to occur. Although twice grain refinement has been successfully predicted by the Karma's model, the theoretical characteristic undercoolings deviate from experimental results. Obviously, the theory that the grain refinement is merely driven by interfacial energy cannot predict the microstructure evolution of $Co_{80}Pd_{20}$ satisfactorily. Comparing the refined morphologies at low (Fig. 3b) and high undercooling (Fig. 3e) reveals that, distinct diversity preserves in the two kinds of refined grains. For the grains refined at lower undercooling, the morphology consists of granular grains, and which is similar to the ripe fragmented dendrite arms. The morphology at higher undercooling consists of equiaxed grains with sharp grain boundaries, in which a large number of defects exist. Considering the fact of the effect of the solute elements and diversity of morphologies, the two kinds of grain refinement can't ascribe to one reason. The Karma's model is inconvenience to interpret the two grain refinements due to which it uniquely attributed the remelting to the liquid/solid interface tension.
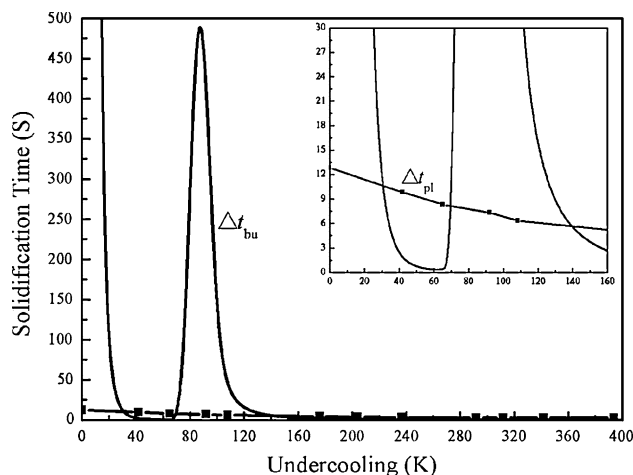
Grain refinement mechanism at low undercooling

It was shown in reference [14], the dendrite remelting can be evaluated by the dimensionless superheating $(\Delta \bar{T}_s')$ of the central part of the dendrites stems (i.e. the initially frozen solid) in recalescence.

$$\Delta \bar{T}_s' = \frac{T_R - T_s'}{\Delta T_0'} \qquad (2)$$

Table 1 Physical parameters of $Co_{80}Pd_{20}$ alloy [33]

Parameter	Symbol	Value
Heat of fusion	ΔH_f (kJ mol^{-1})	12.11
Specific heat of the liquid	C_p (J mol^{-1} K^{-1})	49.2
Diffusion coefficient	D (m^2 s^{-1})	10^{-9}
Thermal diffusivity	α (m^2 s^{-1})	6×10^{-6}
Slope of the liquidus line	m_L (K/at.%)	6.5
Equilibrium partition coefficient	k_0	0.66
Atom space	a_0 (m)	2.54×10^{-10}
Liquid temperature	T_L (K)	1610
Interfacial energy	σ (J m^{-2})	0.25
Speed of sound	V_s (m s^{-1})	4000

Fig. 5 Dendrite break-up time Δt_{bu} (*solid line*) calculated from the Karma model for $Co_{80}Pd_{20}$, *line* with *square symbol* denotes the experimental post-recalescence time Δt_{pl}

where T_R is the highest recalescence temperature corresponding to ΔT, T_s' is the equilibrium solidus temperature corresponding to the compositions C_s' of the central part in the dendrite stems, and $\Delta T_0'$ is the equilibrium crystallization temperature range of the alloy with C_s'. Assuming that the solidification during the recalescence occurs under the adiabatic conditions and the specific heats of the solid and liquid are constant and equal, T_R, T_s', and $\Delta T_0'$ can be calculated from the equations in References [3, 14, 28–30]. The parameters calculation required is listed in Table 1.

The relationship between $\Delta \bar{T}_s'$ and ΔT of $Co_{80}Pd_{20}$ is presented in Fig. 6. With undercooling increasing, the dimensionless superheating $\Delta \bar{T}_s'$ first rises up to its maximum and then descends. The region with maximum $\Delta \bar{T}_s'$ values is located in the undercooling range ΔT_{C1}–ΔT_{C2}, where the initial dendrites in recalescence suffer severe remelting. It indicates that the dendrites solidified in the undercooling range of ΔT_{C1}–ΔT_{C2} have the maximum
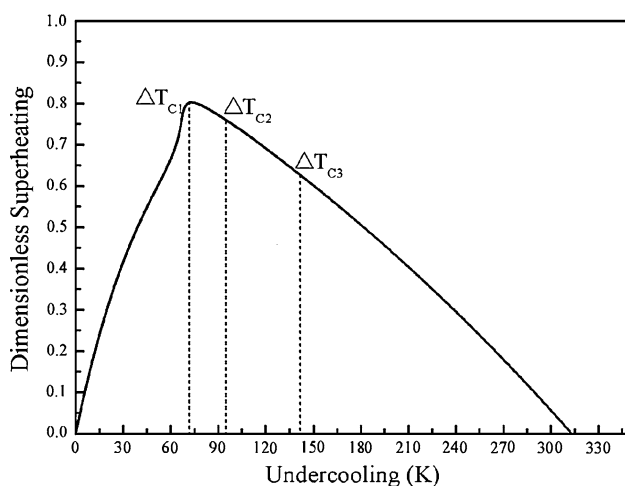
tendency to be remelted, and the grain refinement occurring in this range originates from the break-up of the dendrites under the action of the remelting. Moving from the low undercooling range to increased undercooling, $\Delta \bar{T}'_s$ increases, which makes the dendrites skeleton first be partially remelted (see Fig. 7a), then completely remelted (see Fig. 7b). This further validates that the spontaneous grain refinement that occurs in the range of ΔT_{C1}–ΔT_{C2} is originated from the remelting of the dendrite skeleton.
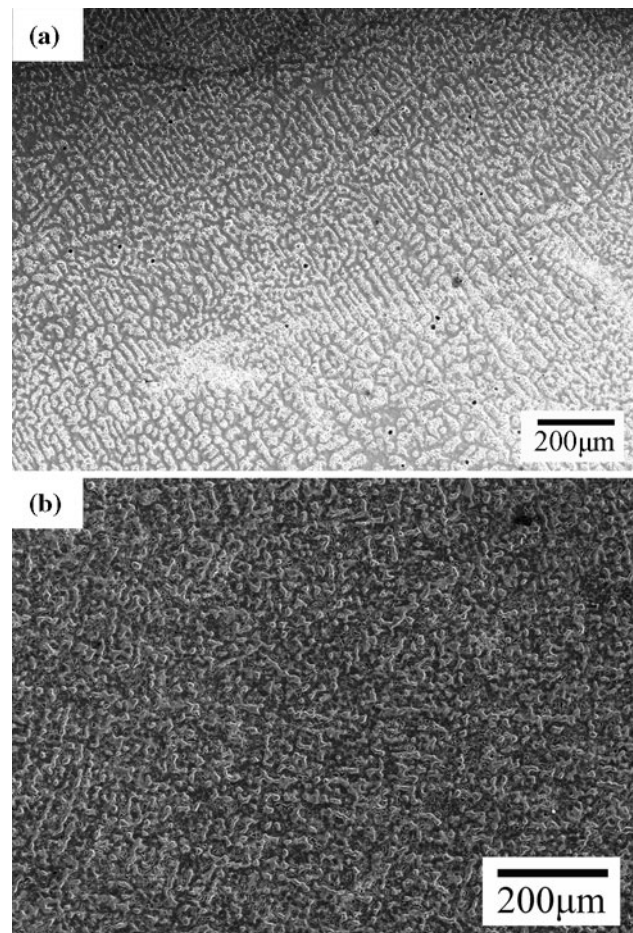
After the dimensionless superheating $\Delta \bar{T}'_s$ rises up to its maximum, with undercooling increasing, the dimensionless superheating $\Delta \bar{T}'_s$ descends monotonously. When undercooling is located within the range of ΔT_{C2}–ΔT_{C3}, the dimensionless superheating decreases to a low level not enough to remelt the initial dendrites. Moreover, the dendrite breakup time (Δt_{bu}) is much longer than the plateau duration time (Δt_{pl}) (in Fig. 5) in ΔT_{C2}–ΔT_{C3}, with grain refinement not having sufficient time to occur. Therefore, the developed directional fine dendrites (Fig. 3c) were remained at this intermediate undercooling range.

Grain refinement mechanism at high undercooling

In contrast, when undercoolings is larger than ΔT_{C3}, the dimensionless superheating of the dendrites in recalescence decreases to a low level, consequently, the remelting is not severe enough to make the dendrites disintegrate into fine crystals. Otherwise, it should not be understood that the dendritic structures in ΔT_{C2}–ΔT_{C3} that were superheated more severely and had to undergo a longer solidification time, still remained at room temperature. The grain refinements at high undercoolings must be induced by other factors rather than remelting. Figures 8, 9 show the substructure in the grains at high undercooling of $Co_{80}Pd_{20}$

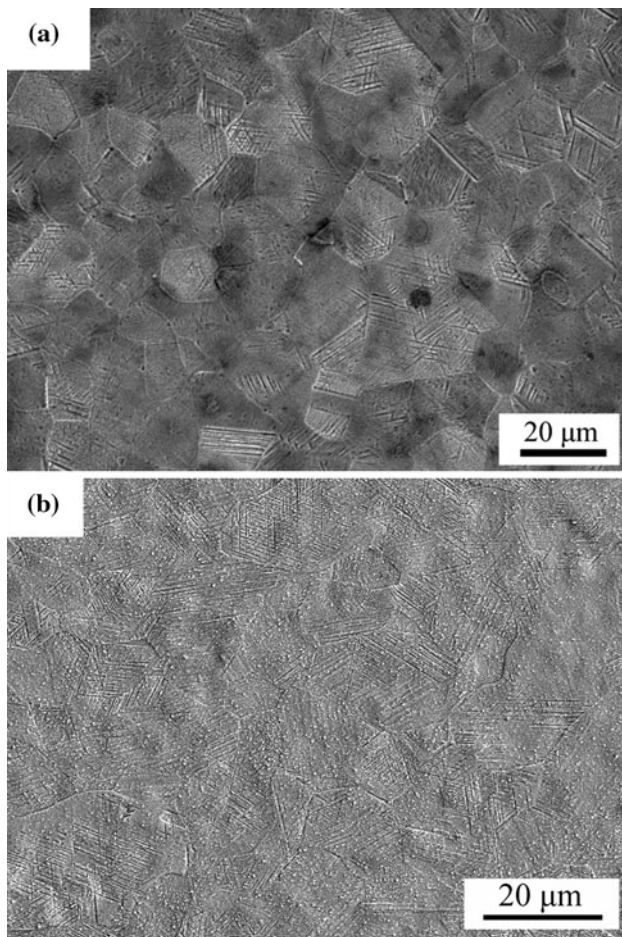Fig. 7 The portion remelted dendrites at undercooling of 65 K (a) and completely remelted dendrites at undercooling of 78 K (b)

alloys. The micrographs reveal a lot of parallel fault ribbons and retiform microstructure formed from intersectant fault ribbons in great mass of grains, and the corner dimension of the intersectant fault ribbons are constants. The analogous substructure has not been detected in other undercooled metallic systems. At the same time, the grain boundary is sharp and straight. These characters further confirmed that, the grain refinement at high undercooling is not originated from the dendrites remelting.
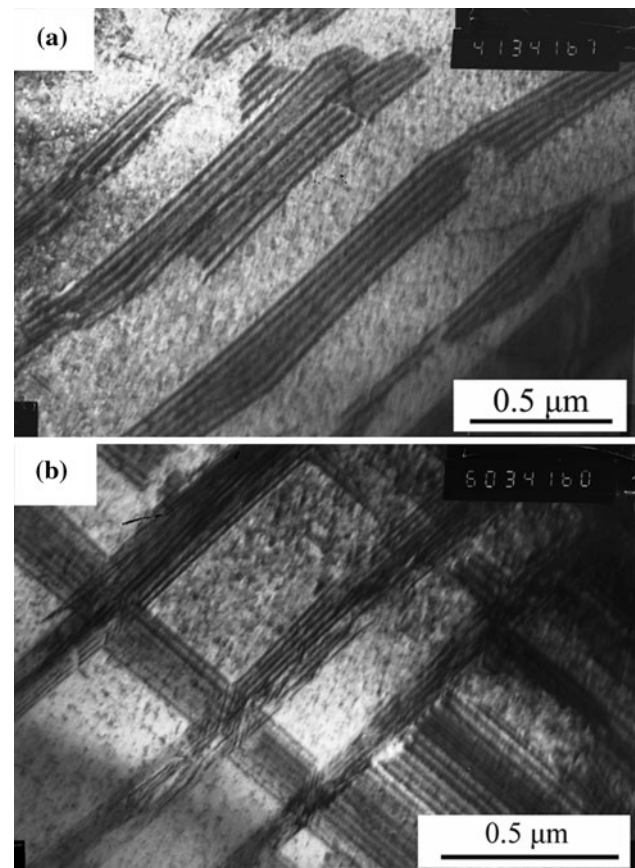
The dense regular fault ribbons are similar to the faults formed by plastic deformation. In normal conditions, the deformation is related to stress. Actually, there is no environment stress loaded on the alloys during the undercooled solidification process. Therefore, the stress should be originated from the rapid solidification process. The stress-induced deformation in the solidification of undercooled $Co_{80}Pd_{20}$ alloy has been discussed in detail in reference [31]. Owing to the average grain, diameter is comparable to the dendrite trunk radius which, in turn, is comparable to the dendrite side-branch spacing. In addition, dense regular faults were detected in the grains at high

Fig. 6 Dimensionless superheating versus undercoolings of $Co_{80}Pd_{20}$ Alloy (ΔT_{C1}, ΔT_{C2}, and ΔT_{C3} denote the three characteristic undercooling)

Fig. 8 The sub-microstructure in the grains at undercooling of 292 K (**a**), 415 K (**b**) (by SEM)

Fig. 9 The sub-microstructure in the grains of $Co_{80}Pd_{20}$ alloy at undercooling of 251 K (by TEM): **a** Parallel stacking faults, **b** intersectant stacking faults

undercooling. In connection with the stress analysis in $Co_{80}Pd_{20}$ [31], we suggest that the grain refinement of $Co_{80}Pd_{20}$ at high undercooling results from stress induced mechanical fragmentation rather than remelting or recrystallization. In the recalescence process, the temperature of the system rose to a high level due to the release of the heat of fusion, the solid phase was annealed. As a result, the boundaries became sharp and straight, at the same time, many high angle boundaries were obtained.

The $Co_{80}Pd_{20}$ alloy shows a low hypercooling limit of 291 K [19]. Such an undercooling is less than the maximum undercooling in present study, i.e., means that hypercooling has been realized in $Co_{80}Pd_{20}$ alloy. On the other hand, there is no abrupt change of the grain sizes and structure morphologies when undercooling exceeds the hypercooling limit (Figs. 3f, 4), i.e., the microstructure evolutions do not change due to the hypercooling. The phenomenon is similar with that observed in Ni–Pd alloys [32].

Conclusions

Within the achieved range of undercooling, 0–415 K, two kinds of grain refinements have been observed in the solidification microstructures and the three characteristic undercoolings are 72, 95, and 142 K respectively. With undercooling increasing, the as-cast microstructure of $Co_{80}Pd_{20}$ alloy can be classified into four types according to the three characteristic undercoolings: coarse dendrites, granular crystals, developed directional fine dendrites, and equiaxed crystals, respectively.

The grain refinement at low undercooling can be attributed to the breakup of dendrite-skeleton originate from the dimensionless chemical superheating-induced remelting. The grain refinement at high undercooling can be ascribed to the stress that originates from the extremely rapid solidification process, which results in the dendrite fragmentation.

The highly developed directional fine dendrite is remained at intermediate undercooling due to the combined conditions of low dimensionless superheating and short

plateau duration time. There is no abrupt change of the grain sizes and structure morphologies when undercooling exceeds the hypercooling limit.

References

1. Herlach DM (1994) Mater Sci Eng R Rep 12:177
2. Walker JL (1959) In: Pierre GRS (ed) The physical chemistry of process metallurgy (part 2), Inter science, New York, p 845
3. Schwarz M, Karma A, Eckler K, Herlach DM (1994) Phys Rev Lett 73:1380
4. Li JF, Yang GC, Zhou YH (1998) Mater Res Bull 33:141
5. Dragnevski K, Cochrane RF, Mullis AM (2004) Mater Sci Eng A 375–377:479
6. Chen YZ, Liu F, Yang GC, Liu N, Yang CL, Xie H, Zhou YH (2008) Mater Charact 59:412
7. Horvay G (1965) Int J Heat Mass Transf 8:195
8. Jackson KA, Hunt JD, Uhlmann DR (1969) J Mater Sci Lett 245:407
9. Liu F, Yang GC, Guo XF (2001) Mater Sci Eng A 311:54
10. Kobayashi KF, Hogan LM (1978) Met Forum 1:165
11. Karma A (1998) Int J Non-Equilibrium Process 11:201
12. Mullis AM, Cochrane RF (1997) J Appl Phys 82:1380
13. Eckler K, Norman AF, Gärtner F, Greer AL, Herlach DM (1997) J Cryst Growth 173:528
14. Li JF, Liu YC, Lu YL, Yang GC, Zhou YH (1998) J Cryst Growth 192:462
15. Chen YZ, Yang GC, Liu F, Liu N, Xie H, Zhou YH (2005) J Cryst Growth 282:490
16. Liu F, Yang GC (2001) J Cryst Growth 231:295–305
17. Holland-Moritz D, Herlach DM, Spaepen F (2007) Superlattice Microst 41:196
18. Massalski TB (1986) Binary Alloy Phase Diagrams. American Society for Metals, Metals Park
19. Wilde G, Görler GP, Willnecker R (1996) Appl Phys Lett 69:2995
20. Schenk T, Holland-Moritz D, Bender W, Herlach DM (1999) J Non-Cryst Sol 250–252:694
21. Albrecht T, Bührer C, Fähnle M, Maier K, Platzek D, Reske J (1997) Appl Phys A 65:215
22. Schenk T, Holland-Moritz D, Herlach DM (2000) Europhys Lett 50:402
23. Herlach DM, Holland-Moritz D, Schenk T, Schneider K, Wilde G, Boni O, Fransaer J, Spaepen F (1999) J Non-Cryst Sol 250–252:271
24. Wilde G, Görler GP, Willnecker R (1996) Appl Phys Lett 68:2953
25. Reske J, Herlach DM, Keuser F, Platzek D (1995) Phys Rev Lett 75:737
26. Herlach DM, Eckler K, Karma A, Schwarz M (2001) Mater Sci Eng A 304–306:20
27. Liu N, Liu F, Yang GC, Chen YZ, Chen D, Yang CL, Zhou YH (2007) Physica B 387:151
28. Boettinger WJ, Coriell SR, Trivedi R (1988) In: Mehrabian R, Parrish PA (eds) Rapid solidification processing: principles and technologies IV. Claitor's, Baton Rouge, p 13
29. Aziz MJ (1982) J Appl Phys 53:1154
30. Piccone TJ, Wu Y, Shiohara Y, Flemings MC (1987) Metall Trans A 18:925
31. Zhou SY, Hu R, Li JS, Chang H, Kou HC, Zhou L (2011) Mater Sci Eng A 528:973
32. Lu SY, Li JF, Zhou YH (2007) J Cryst Growth 309:103
33. Volkmann T, Wilde G, Willnecker R, Herlach DM (1998) J Appl Phys 83:3028